HYDROPHOBIC POLY(VINYLIDENE FLUORIDE) / SILOXENE NANOFILTRATION MEMBRANES

Jing Ji,‡ Saeed Mazinani,‡ Ejaz Ahmed, Y.M. John Chew, Davide Mattia*

Department of Chemical Engineering, Centre for Advanced Separations Engineering, University of Bath, Claverton Down, Bath BA2 7AY, UK

Corresponding author: d.mattia@bath.ac.uk

Abstract

Hydrophobic, chemically resistant nanofiltration (NF) polymeric membranes could provide major improvements to a wide range of processes, from pharmaceutical manufacturing to hazardous waste treatment. Here, we report the fabrication of the first poly(vinylidene fluoride) (PVDF) NF membranes retaining their hydrophobicity and surface chemistry. This was achieved by incorporating in the polymer 2D siloxene, which induce a compaction of the PVDF chains, resulting in low free volume and a highly ordered microstructure. Siloxene nanosheets were obtained from deintercalation of Ca from $CaSi_2$ using HCl, followed by exfoliation and size fractionation, with average lateral dimension of 1 ~ 2 μm and thickness of 3 ~ 4 nm. The resulting membranes, containing 0.075 wt.% of siloxene, have a pure water permeance of 22 ± 2 L m^{-2} h^{-1} bar^{-1} and molecular weight cut-off (MWCO) of 530 Da. The same membrane also showed stable hexane permeance of 11 L m^{-2} h^{-1} bar^{-1} for 24 h with MWCO of around 535 Da. These results supersede the performance of commercial NF membranes, expanding the potential application of nanofiltration to processes requiring stable, chemically resistant and hydrophobic nanofiltration membranes.

Keywords: Siloxene; PVDF membranes; nanofiltration; hydrophobic; organic solvent.

1. Introduction

Nanofiltration (NF) membranes are widely used in a range of separation processes such as water/wastewater treatment, food processing, chemical transformations, textile manufacturing, pharmaceutical production and others [1]. This success is due to a range of characteristics, including high permeance, molecular-scale molecular weight cut-off (MWCO), low energy consumption and operation costs [2]. Most commercial NF membranes are thin film composite (TFC) membranes composed of a thin cross-linked polyamide (PA) separation layer obtained *via* interfacial-polymerisation deposited on a microporous polysulfone membrane support, which is cast on non-woven fabric [1, 3]. PA TFC membranes, however, suffer from a number of limitations, particularly low stability to chlorine [4-6], and selectivity-permeability trade-off [7]. In contrast, polyvinylidene fluoride (PVDF), one of the most commonly used polymeric membrane materials with inherent hydrophobicity, possesses excellent chemical resistance, thermal stability, and mechanical strength [8, 9]. Due to these properties, PVDF membranes now occupy a large market share of commercial microfiltration (MF) and ultrafiltration (UF) membranes, for applications such as drinking water production, pre-treatment for RO systems and wastewater treatment, gas-liquid absorption and membrane distillation [9, 10]. In most cases, PVDF membranes are hydrophilized for better performance in water treatment. There is, however, no commercial PVDF NF membrane available in the market.

Current research on fabrication of PVDF NF membranes can be grouped into two categories, *i.e.,* surface modification and blending modification. In the former, TFC membranes are obtained by forming a NF separation layer on top of a PVDF UF support *via* techniques such as surface coating [3, 11], grafting[12], electrospinning [13], interfacial polymerization [14], cross-linking [15], plasma treatment [16] or electret treatment [17]. For the latter, additives such as functionalized nanomaterials [18, 19] and surfactants [20] have been employed to prepare PVDF NF mixed-matrix membranes (MMMs). In the former case, the PVDF support does not contribute to the NF rejection performance, whereas the majority of the resulting MMMs are more hydrophilic than the bare PVDF membranes. In both cases, the inherent inertness of PVDF is not fully utilized, limiting the potential applications of PVDF NF membranes in harsh conditions *e.g.,* chlorine cleaning or organic solvent nanofiltration.

In this work, a two-dimensional (2D) nanomaterial, siloxene, was used as additive to prepare PVDF NF membranes without compromising the advantageous properties of PVDF material. Siloxene, prepared by deintercalation of Ca from $CaSi_2$, has a 2D corrugated structure composed of Si_6 rings interconnected by Si-O-Si bridges and terminated with hydroxyl groups [21, 22]. Thus far, research on siloxene has focused on its potential applications in photocatalysis, semi-conductors, anodes in batteries, electrodes for supercapacitors, *etc.* [21-24], but not as additives in membrane-based separations. Compared to graphene and graphene oxide, siloxene also have a 2D structure, but are structurally amorphous with good flexibility [21, 22]. Here, siloxene were introduced as an inert additive to alter the internal arrangement of polymer chains in PVDF membranes. The NF feasibility of the PVDF/siloxene mixed matrix membranes (named as PVSi) was assessed by filtrating a series of dye and salt in aqueous and organic solvent solutions using a crossflow filtration setup. It was found that the addition of siloxene successfully extended the application of PVDF membranes to both water and organic solvent NF separations, comparable to commercial NF membranes, without compromising the advantageous surface and physical properties of PVDF membrane.

2. Materials and methods

2.1 Materials

Calcium silicide ($CaSi_2$, technical grade, *Sigma-Aldrich*), hydrochloric acid solution (HCl, purity = 37%, *VWR*) and acetone (purity ≥ 99%, *VWR*) were employed for siloxene synthesis. Polyvinylidene fluoride (PVDF, average Mw ~ 534,000 g mol^{-1}, *Sigma Aldrich*) and N-Methyl-2-pyrrolidone (NMP, purity > 99%, *Acros Organics*) were used for membrane preparation. Various dyes along with four salts (as summarized in Table S5 in the Supporting Information) were used to evaluate the rejection performance of membranes in water and *n*-hexane (purity > 95%, *Fisher Scientific*). All the chemicals were used as received. Deionized (DI) water and ultrapure water (resistivity of 18 MΩ cm^{-1}) were produced using Purelab® Chorus 1 Complete water purification system (Elga LabWater, *Veolia Water Systems LTD*).

2.2 Preparation and characterisation of siloxene

The 2D siloxene nanosheets were synthesized by topochemical transformation of $CaSi_2$ in HCl (Fig. S7 in the Supporting Information) [22]. Briefly, 1 g of $CaSi_2$ powder was mixed with 100 mL of 37% HCl solution at 0 °C for 4 days. During the reaction, Ca was deintercalated from layered $CaSi_2$ and the color of the mixture was changed from black to green. After the reaction, the resultant layered siloxene product was washed with acetone and DI water, followed by exfoliation in an ultrasound bath (40 kHz, *Cole-Parmer*). The obtained siloxene were then subjected to centrifugation at different speeds to achieve desirable size and thickness.

The nanosheet morphology with elemental mapping was investigated by high-resolution TEM (JEM-2100Plus, *JEOL*) with EDS detector (X-Max detector, *Oxford Instruments*) and SAED was also obtained. The average thickness of the nanosheets was measured by AFM (Asylum Research Jupiter XR, *Oxford Instruments*). FTIR analysis was performed on siloxene-embedded KBr pellets using a Frontier FTIR spectrometer (*Perkin Elmer*) and Raman spectra were recorded with a RM1000 Raman Microscope (*Renishaw*) at 532 nm. XRD (D8-Advance PXRD, *Bruker*) with Cu Kα1 radiation source was operated at 40 kV and 40 mA (0.015° step size) to examine the crystallinity and phase of the siloxene powders. XPS was performed using a K-alpha+ spectrometer (*Thermo Fisher Scientific*) with survey scans recorded at 150 eV (1 eV step size) and high-resolution scans at 40 eV (0.1 eV step size).

2.4 Preparation of PVSi membranes

The mixed-matrix PVDF NF membranes were prepared using the phase inversion technique. Siloxene was first dispersed in NMP with controlled concentration by solvent exchange, after which a certain amount of PVDF was dissolved in the nanosheet suspension to prepare dope solutions with different compositions, as shown in Table 1. The dope solution was left overnight to de-gas, and the dope solution was then cast on a glass plate with thickness of 50 μm. The nascent polymer film was exposed to air for 15 s to let solvent partially evaporate. The cast film was then immersed in a water coagulation bath. Water was changed regularly to remove any residual solvent.

Table 1. Dope compositions for the PVDF/siloxene mixed matrix membranes.

Membranes	PVDF (wt.%)	NMP (wt.%)	Siloxene (wt.%)
PVSi-0	17.500	82.500	0
PVSi-025	17.500	82.475	0.025
PVSi-050	17.500	82.450	0.050
PVSi-075	17.500	82.425	0.075
PVSi-100	17.500	82.400	0.100
PVSi-150	17.500	82.350	0.150

2.5 Characterization of PVSi membranes

The membrane cross-sectional morphologies were investigated by FE-SEM (JSM-6301F, *JEOL*). Membrane samples were fractured in liquid nitrogen to retain their cross-section structures. All the samples were sputter-coated with chromium of 10 nm thickness prior to SEM observation.

Hydrophilicity of the membranes was assessed using water contact angle goniometer (OCA15, *Date Physics*) in sessile mode at room temperature. 1 μL droplets of water were used and the values reported are the average of ten measurements at different positions.

The surface zeta potential of each membrane sample was measured using a Zetasizer Nano (ZS, *Malvern Instruments Ltd*.) with the surface ζ accessory at neutral pH = 7.0. A tracer solution was prepared by adding a low concentration of polystyrene in 10 mM NaCl solution. Each sample was measured at least three times and the reported values were the average of the measurements.

The surface roughness of the membrane samples was assessed by AFM (AFM Multimode IIIA, *Bruker*) in tapping mode over scan areas of 5×5 μm^2.

ATR-FTIR (Frontier, *Perkin Elmer*) was employed to characterize the chemical bonds on the membrane surface. The spectra were collected in the wavenumber range of 4000 to 600 cm^{-1} by accumulating 10 scans at a resolution of 4 cm^{-1}.

The distributions of siloxene on membrane surfaces were investigated by Raman mapping (RM1000 with inVia system, *Renishaw*) at 532 nm [25]. Areas of 100 × 100 μm^2 were scanned on each membrane sample with the line mapping technique.

XRD (D8-Advance PXRD, *Bruker*) with Cu Kα1 radiation source (1.5406 Å) was operated at 40 kV and 40 mA (0.015° step size) to examine the compactness of the PVSi membrane samples. The obtained spectra were analyzed using CrystalDiffract software (*CrystalMaker Software Ltd, UK*). 2θ values are reported in Table 3 with 4 significant figures for ease of readability, whereas the original values have 6.

The melting behavior of each membrane sample was characterized using differential scanning calorimetry (DSC Q20, *TA Instruments*). The samples were heated from room temperature (~ 20 °C) to 220 °C with a ramping rate of 10 °C min^{-1}. The percentage crystallinity of PVDF in each sample was determined by

$$\boldsymbol{crystallinity}\ (\%) = \frac{\boldsymbol{\Delta H_m}}{\boldsymbol{\Delta H_m^0}} \times \mathbf{100}\% \qquad (1)$$

where ΔH_m is the enthalpy associated with membrane melting and ΔH^0_m is the theoretical melting enthalpy of 100% crystalline PVDF, which is 104.7 J g^{-1}. The reported data were the average of three measurements taking from the same membrane sample.

The dynamic mechanical properties of the membrane samples were analyzed using dynamic thermo-mechanical analysis (DMA1, *Mettler Toledo*) in auto-tension mode. The samples were cut into 20 × 5 mm^2 strips. The sample strips were heated from – 80 °C to 145 °C with ramping rate of 3 °C min^{-1} in air. The data recorded were the average of three measurements.

2.6 Performance of PVSi membranes

Pure water and hexane permeation tests were conducted using a dead-end filtration cell (*Sterlitech Corporation*) connected with a 5 L feed tank. The operating pressure was fixed at 2 bar with compressed air. All the samples were compacted for 3 h prior to sample collection. The permeance, K (L m^{-1} h^{-1} bar^{-1}), of the membrane was calculated by using Equation 2:

$$\boldsymbol{K = \frac{V}{\Delta t \Delta p A}} \quad (2)$$

where K is the permeance, V is the permeate volume, A is the effective membrane area (*i.e.,* 14.6 cm^2), Δt is the time for permeate collection and Δp is the operating pressure (*i.e.,* 2 bar). After the pure water or solvent test, the membrane sample was transferred into a cross-flow cell for the rejection tests of different dyes and salts. The concentrations of all the dye feed solutions were 0.01 g L^{-1}, whereas the concentrations of salt solutions were 1 g L^{-1} except for NaCl, which was 2 g L^{-1}. The concentrations of dyes and salts in the feed, permeate and retentate solutions were measured by UV-visible spectrophotometer (Cary 100, *Agilent*) and conductivity meter (*Thermo Fisher*), respectively. The rejection of the tracer was calculated using Equation 3:

$$R = \left(1 - \frac{C_p}{C_f}\right) \times 100\% \quad (3)$$

where R is the rejection, C_p and C_f are the tracer concentrations in the permeate and feed solutions, respectively. The mass balance for each rejection test was also calculated according to

$$mass\ balance\ (\%) = \frac{C_p V_p + C_r V_r}{C_f V_f} \times 100\% \quad (4)$$

where C_r is the tracer concentration in the retentate solution, V_p, V_r and V_f are the volume of permeate, retentate and feed solutions, respectively. Representative UV-vis spectra and photographs of feed, retentate and permeate can be found in Fig. S8. For all the filtration/separation tests, at least three samples were tested for each membrane and the average value was recorded.

2.7 Estimation of dyes hydrated radii

The chemical structures of the dyes were first drawn using ChemDraw Professional 19.1 (*PerkinElmer*) and then imported into Chem3D. The CAA of each structure was computed using the Molecular Mechanics 2 Minimize Energy method which considers a sphere with a radius of 1.4 Å. Minimum root mean square gradient was set to be 0.1. The hydrated radius of each dye was then estimated based on the correlation between CAA and hydrated radii [26, 27].

3. Results and discussion

3.1 Characterization of siloxene

The 2D siloxene were synthesized by deintercalation of Ca from $CaSi_2$ using HCl, followed by exfoliation and size fractionation. The morphological characteristics of the exfoliated siloxene were studied by transmission electron microscopy (TEM). Fig. 1a and Fig. 1b show that the nanosheets have an average lateral dimension of 1 ~ 2 μm and have a high degree of transparency, uniform and homogeneous contrast, which indicate their ultrathin nature. Few layered siloxene were also observed, likely due to the surface tension of the solvent pulling nanosheets into close contact during the drying process for sample preparation, similar to what observed for boron nitride nanosheets [28]. The selected-area electron diffraction (SAED) pattern in the inset illustrates that the siloxene are mainly amorphous, with no coherent scattering domains observed [29]. The elemental mappings obtained from energy dispersive X-ray spectroscopy (EDS) demonstrates the uniform distribution of Si and O atoms throughout the siloxene (Fig. 1c and Fig. 1d). The atomic force microscopy (AFM) micrograph (Fig. 1e) of the nanosheets dispersed on silicon wafer presents a 2D structure with lateral size comparable to that measured by TEM. As shown in the height profile (Fig. 1f), the average thickness of the siloxene is 3 ~ 4 nm, which is equivalent to 4 ~ 6 layers [30] and coincides with observations from TEM (Fig. 1a).

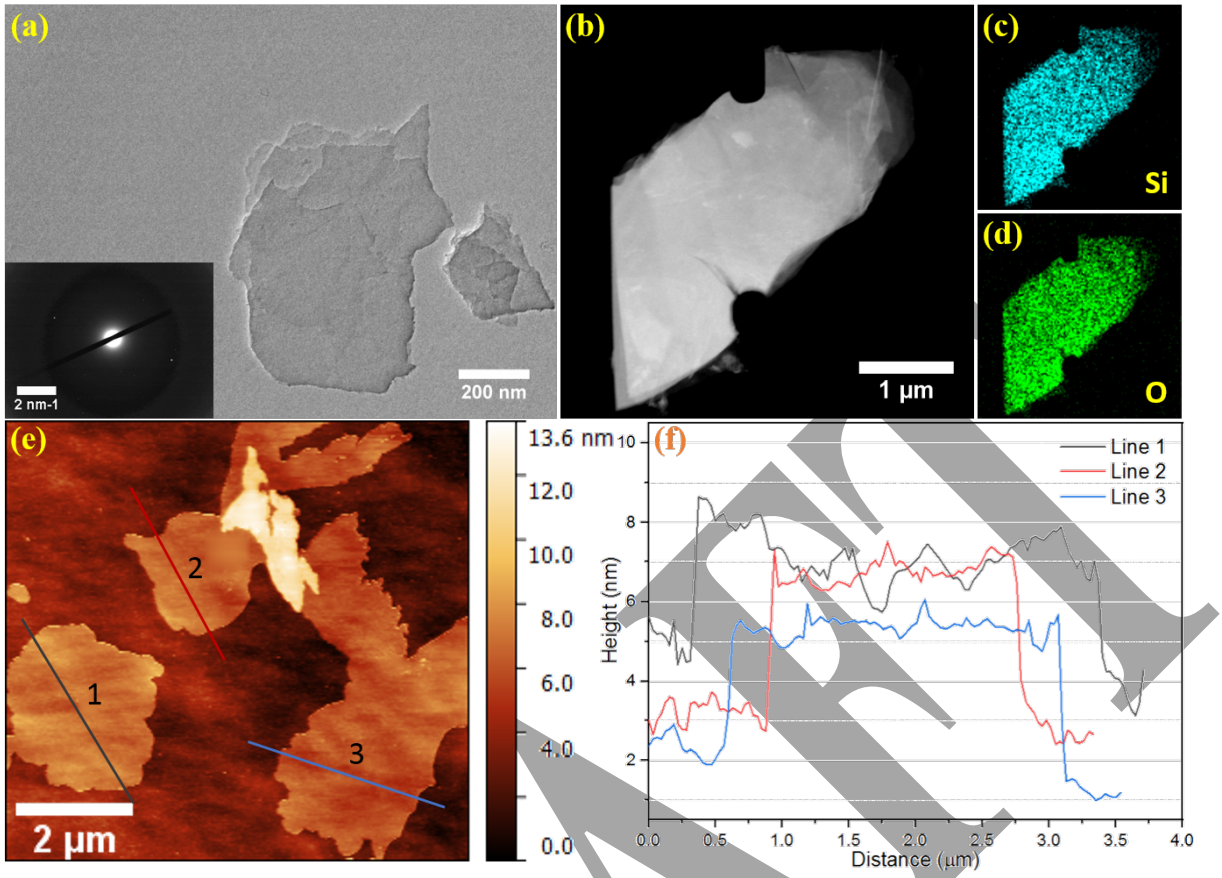

Fig. 1. Morphological characterisations of the exfoliated siloxene: (a, b) TEM (inset of (a): SAED pattern); (c, d) EDS mapping of (b); (e) AFM and (f) height profile of three nanosheets in (e).

Fourier transform infrared (FTIR) was performed to investigate the chemical bonds in the siloxene. As shown in Fig. 2a, the characteristic bands observed at 437 cm^{-1}, 874 cm^{-1}, 1061 cm^{-1}, 1630 cm^{-1}, 2140 cm^{-1}, 2250 cm^{-1}, and 3400 cm^{-1} correspond to vibrations of ν(SiSi), ν(SiH), ν(SiOSi), ν(SiOH), $\nu(OSi_2SiH)$, $\nu(O_3SiH)$ and ν(OH), respectively.[22, 31] The presence of $\nu(OSi_2SiH)$ and absence of $\nu(Si_3SiH)$ (~ 2100 cm^{-1}) and $\nu(O_2SiSiH)$ (~ 2200 cm^{-1}) indicates the Kautsky-type structure of siloxene, which means that the Si planes in the nanosheets are mainly composed of Si_6 rings interconnected by Si–O–Si bridges.[31, 32] The broad band around 3400 cm^{-1} is attributed to the hydroxyl groups at the edges and surface of the siloxene formed by oxidation and hydroxylation during the synthesis reaction.[22, 32] Raman spectrum of siloxene is displayed in Fig. 2b, which clearly shows the presence of Si–Si vibrations (370 cm^{-1} and 517 cm^{-1}), Si–O vibration (494 cm^{-1}) and Si–H vibrations (638 cm^{-1}, and 733 cm^{-1}) [21, 22]. The peaks at 370 cm^{-1} and 517 cm^{-1} and the small shoulder at ~ 410 cm^{-1} are ascribed to the corrugated Si (111) planes in siloxene [33]. X-ray

diffraction (XRD) was performed to analyze the potential crystal structure of siloxene. The XRD pattern in Fig. 2c shows no sharp diffraction peaks, which coincides with the amorphous nature of siloxene detected by SAED. On the other hand, two broad peaks at 24.3° and 47.5° are characteristic 2D peaks, corresponding to the Si (100) and (110) planes [31, 34]. This might be explained by the re-stacking of nanosheets in the dry and powdered siloxene sample. Therefore, the XRD data suggested that the synthesized siloxene product was successfully exfoliated into individual nanosheets, which were restacked as a-few-layer units [30].

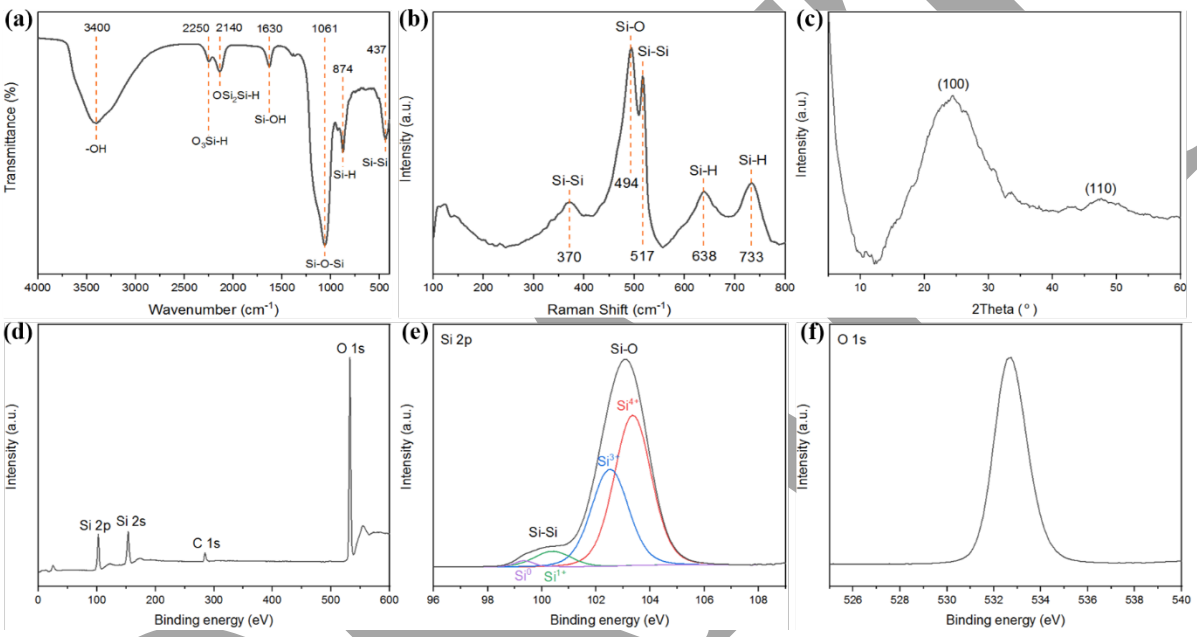

Fig. 2. Spectra of siloxene: (a) FTIR; (b) Raman; (c) XRD; (d) XPS survey scan; XPS high-resolution scans of (e) Si 2p and (f) O 1s.

X-ray photoelectron spectroscopy (XPS) was performed to investigate the chemical states of the elements in siloxene. The survey scan of siloxene in Fig. 2d shows the presence of silicon (102.3 eV and 153.8 eV), oxygen (532.7 eV) and adsorbed carbon impurities (284.7 eV). High-resolution scans of Si 2p and O 1s were also conducted to study the oxidation state of Si. The core-level spectrum of Si 2p is presented in Fig. 2e and has two peaks at 100.1 eV and 103.1 eV corresponding to Si of 2D network and oxidized Si, respectively [31]. In addition, four peaks could be deconvoluted from the Si 2p spectrum at binding energies of 99.4 eV, 100.4 eV, 102.6 eV and 103.4 eV, which are assigned to Si^{0}, Si^{1+}, Si^{3+} and Si^{4+} oxidation states, respectively [35]. Fig. 2f displays the high-resolution scan

of O 1s with a peak at 532.7 eV referring to the Si-O bond. The results of XPS analysis provides direct evidence that the Si in the nanosheets are connected by Si-O-Si bridges and terminated with hydroxyl functional groups,[21, 22] confirming the integrity of the siloxene after exfoliation.

3.2 Characterization of PVSi membranes

The obtained siloxene was employed as an additive to prepare PVDF mixed matrix membranes. The pure PVDF membrane control sample is named as PVSi-0, and the MMMs are labelled as PVSi-025, PVSi-050, PVSi-075, PVSi-100 and PVSi-150 corresponding to the different loadings of siloxene (0.025, 0.01, 0.075, 0.1 and 0.15 wt.%). Fig. 3a shows the field emission scanning electron microcopy (FESEM) micrograph of the overall cross-sectional structure of PVSi-075, which is representative of all other PVSi membranes (Fig. S1 in the Supporting Information), all (with or without siloxene addition) possessing a similar asymmetric structure [36, 37]. Generally, the membranes are composed of a porous sublayer containing macrovoids [37] extending from the skin layer to the bottom and a ~ 100 nm dense top layer (Fig. 3a) with an overall thickness of around 20 ± 1 µm (analyzed with Image J).

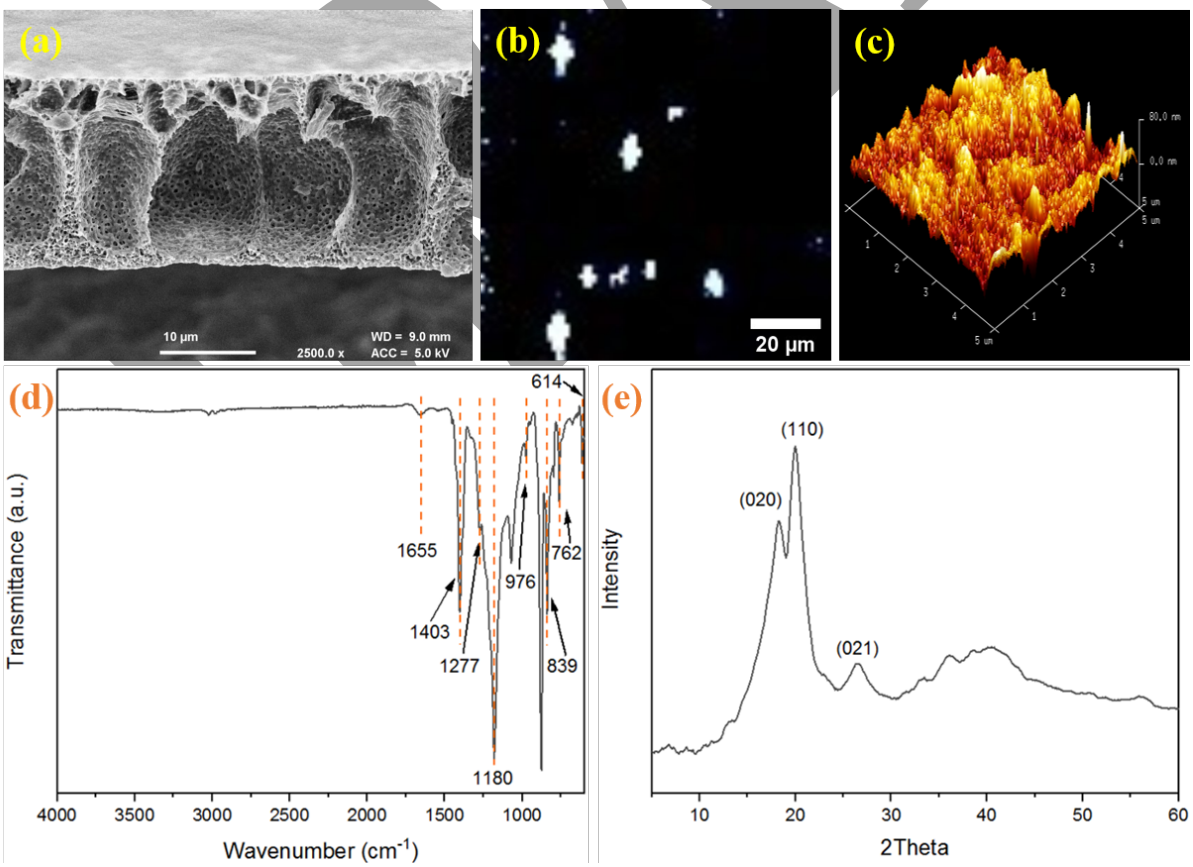

Fig. 3. Characterizations of PVSi-075 membrane: (a) FESEM micrograph of membrane cross section; (b) Raman mapping of the distribution of siloxene on membrane surface (the bright pixels represent the location of siloxene); (c) AFM micrograph of membrane surface; (d) FTIR-ATR spectrum and (e) XRD spectrum.

When investigating MMMs, the distribution of inorganic additives in the polymer matrix is crucial since fillers tend to form agglomerates leading to phase separation and hence, poor properties and performance [38, 39]. Here the distribution of siloxene in the PVSi membranes was investigated *via* Raman mapping (Fig. 3b and Fig. S2 in the Supporting Information), where the Raman intensity at ~ 519 cm^{-1} was marked as bright spots. Larger amounts of siloxene were detected on the PVSi membranes' surface as the siloxene loading increased. In addition, large agglomerates of the nanosheets were observed for PVSi-100 and PVSi-150 samples, suggesting that there is a threshold loading of siloxene in PVDF membrane beyond which agglomeration occurs, in agreement with most literature on MMMs [25]. The existence of siloxene agglomerates on the membrane's surface would decrease the compatibility between the polymer and the nanosheets, which, in turn, could lead to a heterogenous distribution of the inorganic fillers and the formation of defects/voids.[9, 40] In MMMs using other 2D materials, this has resulted in an increase in solvent flux but reduction in the rejection performance [25], as indeed observed for the PVSi-100 and PVSi-150 membranes, as discussed in the following section.

The AFM micrographs in Fig. 3c and in Fig. S3 in the Supporting Information show the surface morphologies of PVSi membranes. As summarized in Table 1, there is no obvious change in the membranes' surface roughness upon addition of different amounts of siloxene. Similarly, the addition of siloxene did not modify the wetting behavior, surface charge, melting temperature nor degree of crystallinity compared to the pure PVDF membrane. This is critical, as the sought-after characteristics of PVDF (chemical inertness, negative surface charge and high contact angle) are preserved with the addition of siloxene, which, however, enables making PVDF membranes in the nanofiltration range. Compared to other membrane samples, PVSi-075 showed a slight difference, including relatively lower contact angle and surface roughness, but higher surface zeta potential, melting temperature and crystallinity degree. However, the data are all within experimental error and no definite relationships could be established between the siloxene loading amount and the physical properties of the

membranes. On the other hand, Young's Modulus and storage modulus (Table 2) of the PVSi membrane show a clear increasing trend as the siloxene loading amount increases. In particular, with the maximum 0.15 wt.% siloxene added, the Young's modulus and storage modulus increased from 63.1 ± 0.8 MPa to 94.0 ± 2.2 MPa and from 62.7 ± 0.8 MPa to 93.7 ± 2.2 MPa, respectively. Similar findings have been reported for other PVDF MMMs [8, 41].

Table 2. Summary of the physical properties of PVSi membranes.

Sample	Water Contact Angle (°)	Surface Zeta Potential (mV)	R_a (nm)	R_q (nm)	Melting Temperature (°C)	Degree of Crystallinity (%)	Young's Modulus (MPa)	Storage Modulus (MPa)
PVSi-0	85 ± 2	-70.9 ± 3	11.6 ± 1.5	14.7 ± 1.5	147 ± 2	55 ± 1	63.1 ± 0.8	62.7 ± 0.8
PVSi-025	83 ± 2	-73.3 ± 4	11.8 ± 1.2	14.7 ± 1.6	146 ± 1	54 ± 3	64.4 ± 3.3	64.0 ± 3.4
PVSi-050	82 ± 2	-72.3 ± 3	10.5 ± 1.3	13.5 ± 1.5	146 ± 1	53 ± 3	71.7 ± 0.9	71.3 ± 0.9
PVSi-075	79 ± 3	-71.7 ± 3	10.8 ± 1.1	13.8 ± 1.3	148 ± 3	55 ± 3	72.1 ± 0.9	71.7 ± 0.9
PVSi-100	84 ± 2	-72.2 ± 3	10.6 ± 0.5	13.3 ± 0.5	147 ± 2	56 ± 1	78.2 ± 1.3	77.8 ± 1.2
PVSi-150	85 ± 2	-71.6 ± 4	11.6 ± 2.7	14.6 ± 3.1	146 ± 1	56 ± 3	94.0 ± 2.2	93.7 ± 2.2

Attenuated total reflection FTIR (ATR-FTIR) on the PVSi membranes was conducted to study the surface chemistry. As shown in Fig. 3d and Fig. S4 in the Supporting Information, all the membrane samples show mainly the typical spectra of PVDF. For example, the characteristic peaks at 1403 cm^{-1} and 1180 cm^{-1} are assigned to the $-CF_2$ deformation and stretching vibration bonds [42]. The bands at 976 cm^{-1}, 762 cm^{-1} and 614 cm^{-1} are the characteristic of α phase absorption, and β phase can be identified from the peak at 839 cm^{-1} and the shoulder at 1277 cm^{-1} [43]. Comparing all the spectra (Fig. S4 in the Supporting Information), a small new peak at 1655 cm^{-1} appeared in the spectra of sample PVSi-075, PVSi-100 and PVSi-150, and it could be ascribed to the Si−OH stretching vibration. Meanwhile, the absence of the *ν*(OH) vibration in siloxene at 3400 cm^{-1} indicates that the addition of siloxene had little effect on the surface hydrophobicity of PVSi membranes, which is consistent with the water contact angle data in Table 1. In contrast, the surface chemistry of the PVSi MMMs were not changed by the incorporation of nanosheets, which means that the chemical resistance of PVDF material is successfully retained upon the addition of siloxene.

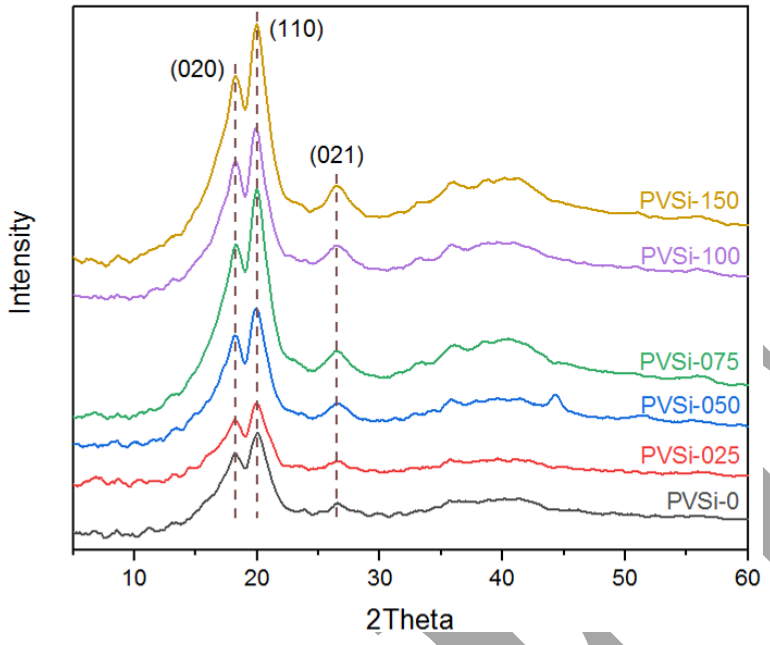

Fig. 4. XRD patterns of all PVSi membrane samples.

XRD was employed to investigate the effect of siloxene on the PVDF polymer at the molecular scale, hence, to evaluate chain ordering in the mixed matrix membranes. The XRD patterns of all the PVSi membranes are shown in Fig. 4, and the interpretation of the patterns is summarised in Table 2 (all the data listed in Table S1 in the Supporting Information). The three intense diffraction peaks at 18.3º, 19.9º and 26.5º appearing in all the membrane samples correspond to α-phase PVDF crystal [41, 43] The two broad XRD peaks of siloxene at 24.3° and 47.5° could not be clearly observed for any of the PVSi membrane samples due to overlapping of the peaks (Fig. 4). As shown in Table 2, there are only tiny changes in the 2θ location of the PVSi membranes for (020) and (110) peaks, whereas the 2θ of the (021) peak shifts to higher values as the siloxene loading amount increases. The *d*-spacing values for each diffraction peak of all the PVSi membranes have been calculated since *d*-spacing can provide a possible approach to evaluate the inter-segmental distance between polymer backbones, *i.e.,* a tighter polymer chain structure normally has a smaller *d*-spacing value [44] It has also been found that polymers with smaller *d*-spacing tend to have less fractional free volume [45]. As shown in Table 3, the PVSi-075 membrane possesses the smallest *d*-spacing of 3.30 Å for the PVDF α-phase (021) plane compared to other membranes, suggesting that the PVSi-075 membrane has the tightest (most compacted) structure. For a deeper investigation, the chain ordering of the PVSi membranes were further analysed in term of the half-width to height ratio (HW/H) of the diffraction peak (Table

2), which reflects the chain ordering in the polymer matrix [46]. Smaller HW/H values mean higher chain ordering. Generally, the PVDF polymer chains inside the PVSi membranes became more ordered in the (020) and (021) planes with increasing siloxene loading. In particular, the PVSi-075 membrane shows the highest ordering of polymer chains in the (110) plane with the smallest HW/H value of 0.002. Both the smallest *d*-spacing value for the (021) plane and the smallest HW/H value for the (110) plane suggest that the PVSi-075 membrane has the most compacted polymer chain structure with least fractional free volume and highest chain ordering at the molecular scale. Such chain structure highly contributes to the filtration performance of PVSi-075 membranes, which will be discussed in the following section. The potential molecular interaction between siloxene and PVDF polymer could be hydrogen bonding between hydroxyl group from the nanosheets and fluorine atoms from PVDF [47] and dipole-dipole attraction between oxygen atoms of siloxene and C–H groups of the polymer [48].

Table 3. XRD pattern analysis of PVSi membranes.

Sample Name	(020)			(110)			(021)		
	2θ (°)	*d*-spacing (Å)	HW/H[a)]	2θ (°)	*d*-spacing (Å)	HW/H	2θ (°)	*d*-spacing (Å)	HW/H
PVSi-0	18.31	4.84	0.008	19.94	4.44	0.004	26.54	3.38	0.012
PVSi-025	18.31	4.84	0.007	19.94	4.44	0.004	26.65	3.34	0.010
PVSi-050	18.32	4.84	0.006	19.94	4.44	0.004	26.72	3.33	0.009
PVSi-075	18.32	4.83	0.005	19.95	4.43	0.002	26.97	3.30	0.007
PVSi-100	18.32	4.83	0.005	19.95	4.43	0.003	26.78	3.32	0.007
PVSi-150	18.32	4.83	0.005	19.95	4.43	0.003	26.81	3.32	0.007

[a)]: ratio of half-width to height.

3.3 Filtration performance of PVSi membranes

NF membranes are typically able to reject solutes with molecular weight below 1000 Da, so the NF feasibility of the PVSi membranes was first assessed by filtration of Rose Bengal dye (RB, Mw = 1017.64 Da) solution. Fig. 5a compares the water permeances and dye rejections of RB for all PVSi membranes (mass balance above 95% for all tests). It is observed that the addition of siloxene first

decreases the water permeance of the PVSi membranes and then increases slightly after the loading amount was more than 0.075 wt.%. However, such permeance increase is marginal and therefore any further increase in loading is not beneficial. The PVSi-0 (pristine PVDF) membrane shows the highest water permeance of 100 ± 2 L m^{-1} h^{-1} bar^{-1}, while PVSi-075 has the lowest water permeance of 22 ± 2 L m^{-1} h^{-1} bar^{-1}. On the other hand, the filtration results indicate that the RB rejection improved from 52 ± 1% (PVSi-0) to 94 ± 3% (PVSi-075). It should be noted that membranes with loadings higher than 0.075 wt.% (PVSi-100, PVSi-150) show relatively poor reproducibility, which could be attributed to the agglomeration of siloxene forming defects on membrane surface (Fig. S2 in the Supporting Information), a known issue in MMMs [25]. The MWCO, defined as the lowest molecular size of the solute of which 90% is retained by the membrane, was used to further characterize the filtration performance of the PVSi membranes. Among all the PVSi membranes, only the PVSi-075 membrane with pure water permeance of 22 ± 2 L m^{-1} h^{-1} bar^{-1} and RB rejection of 94 ± 3 %, shows NF performance while other membranes are showing UF performance. Such high rejection of PVSi-075 membrane could be attributed to its highly compacted polymer chains with low fractional free volume and high chain ordering in the polymer matrix, as discussed earlier.

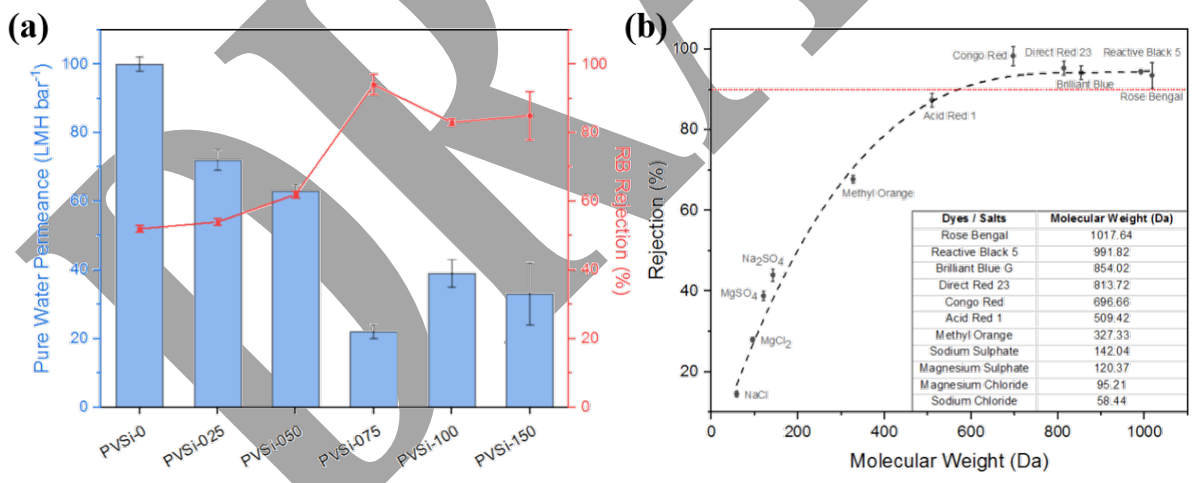

Fig. 5. Filtration performance of PVSi membranes: (a) pure water permeance (columns) and RB rejection (orange dots; lines do not indicate trends but only to provide visual guide) for all the PVSi membranes; (b) rejection of PVSi-075 membrane for various dyes and salts in water (red dotted line refers to 90% rejection; the inset table summarizes the molecular weight of each tracer; mass balance has been calculated for all the rejection tests and was above 95% for all the tests).

The NF performance of the PVSi-075 membrane was further evaluated by using a series of dyes with different molecular weights ranging from 58.44 to 1017.64 Da. Fig. 5b shows that the PVSi-075 membrane displays very high rejections (> 94 %) for RB, Reactive Black 5 (RB5), Brilliant Blue (BB), Direct Red 23 (DR23) and Congo Red (CR) dyes, slightly lower rejection for Acid Red 1 (AR1) (87 ± 2 %) and low rejection (68 ± 1 %) for Methyl Orange (MO). These data suggest that the MWCO of the PVSi-075 membrane is around 530 Da. It is worth noting that the adsorption of the dyes into the membrane is negligible since the mass balance for all the tests are more than 95% (Table S2 in the Supporting Information). Calibration curves for the measurements are reported in Fig. S5 in the Supporting Information.

Generally, size (steric) exclusion and Donnan (charge) exclusion are the main rejection mechanisms in NF [49, 50]. As all the membranes have comparable negative surface zeta potential, regardless of siloxene loading, they will have similar electrostatic repulsions for the same dye. As such, while charge rejection is likely to occur, given the negative charge of the dyes tested, any difference between the membranes can be convincingly attributed to size rejection. The PVSi-075 membrane exhibits higher rejection for CR (Mw = 696.66 Da, R = 98 ± 2 %) with lower molecular weight compared to RB (Mw = 1017.64 Da, R = 94 ± 3 %). Careful considerations including the dye structures in relation to their shape, flexibility and compactness are required to explain the observed membrane rejections. To this aim, the hydrated radius (Rh), which reflects the apparent size (physical size) of the dye molecule [51], has been considered. Several methods have been used to estimate the hydrated radii of dyes using a correlation between more easily obtainable size parameters (*e.g.,* Stokes and crystal radius) [26, 52] and physical parameters (*e.g.,* viscosity with hydration radius) [53, 54]. Solute transport is strongly hindered when the pore size of a membrane is smaller than the hydrated radius.[55] Connolly Accessible Area (CAA) is defined as the locus of the center of the solvent molecule while it is rolled around the probe molecule's van der Waals surface [56, 57]. A correlation (Fig. S6 in the Supporting Information) was established between CAA and the hydrated radii of various dye molecules (Table S3 in the Supporting Information) [51, 58]. The hydrated radii of the dyes used in this work were then estimated from this correlation, as summarized in Table S4 in the Supporting Information. As shown in Fig. 6, compared to RB5, BB, DR23 and CR, Rose Bengal has a smaller hydrated radius although it has the largest molecular weight among all the dyes (insert table

in Fig. 5b). Moreover, a closer look at the structure of the dyes reveals that the presence of centered/close conjugated rings reduces the flexibility of the molecules. This suggests that RB, AR1 and MO have almost spherical shape, whereas the other dyes are more elongated. According to Fig. 6, the cut-off of the PVSi-075 membrane corresponds to the hydrated radius of 5.89 Å.

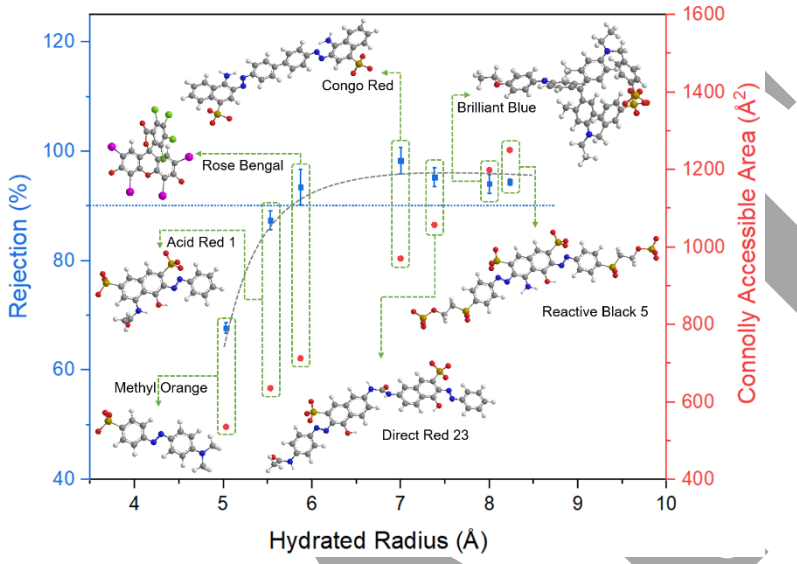

Fig. 6. Dye rejections (blue) of PVSi-075 membrane based on the 3D chemical structure and hydrated radius calculated from CAA (red).

The separation performance of PVSi-075 membrane for hexane as a non-polar solvent was further studied in terms of pure solvent permeance and dye rejection. The results revealed that pure hexane permeance is around 11 ± 2 L m^{-1} h^{-1} bar^{-1} for 24 hours, which is higher than commercial TFC NF membranes and is comparable to the best organic solvent nanofiltration (OSN) membranes in the literature [59-61]. Moreover, the PVSi-075 membrane sample shows 47 ± 1 % rejection for Sudan IV (Mw = 380.44 Da) and 89 ± 1 % rejection for Hexaphenylbenzene (Mw = 534.69 Da). These data suggest that the MWCO of the PVSi-075 membrane in hexane could be around 535 Da, which is similar to the MWCO in water (530 Da). Considering the different structure of the tracers, the results indicate that there is nearly no change to the structure of the PVSi-075 membrane in hexane and therefore the membrane is a very promising candidate for organic solvent nanofiltration application involving non-polar solvents.

The desalination performance of the PVSi-075 membrane was also investigated by the filtration of monovalent (NaCl) and divalent salts (Na_2SO_4, $MgSO_4$ and $MgCl_2$). As shown in Fig. 5b and Table S2 in the Supporting Information, the PVSi-075 membrane showed retention between 15 ~ 44 % for the studied salts. The results for salt rejection tests followed the order of Na_2SO_4 > $MgSO_4$ > $MgCl_2$ > NaCl. This observation could be explained by size exclusion effect [62]. Similar results have been reported in the literature for other NF membranes [63-65]. Compared with NaCl, the divalent salts Na_2SO_4, $MgSO_4$ and $MgCl_2$ possess larger molecular sizes [26, 27], thus providing higher resistance to passage through the membrane. The monovalent over divalent ion selectivity (α) is of interest for NF applications to allow the retention of divalent ions without the need to pay for the osmotic pressure penalty of NaCl [66], The α value for the PVSi-075 membrane is 1.39 which is comparable with literature values for TFC NF membranes [66]. The mass balance for the salt rejection experiments was above 95% for all samples.

4. Conclusions

This paper demonstrates the successful preparation of PVDF/siloxene mixed matrix NF membranes with good pure water permeance and remarkable dye rejection in water and in hexane. The dye filtration results revealed that among all the compositions tested, only PVSi-075 showed NF performance where the RB rejection was above 90% with pure water permeance of 22 ± 2 L m^{-1} h^{-1} bar^{-1}. The MWCO of the PVSi-075 membrane is determined to be around 530 Da. Furthermore, the PVSi-075 membrane showed stable hexane permeance of 11 L m^{-1} h^{-1} bar^{-1} for 24 h. Such outstanding performance could be attributed to the polymer chains becoming highly compacted with low fractional free volume and high ordering caused by the introduction of siloxene. In particular, the surface and physical properties of PVDF membranes were successfully retained upon the addition of siloxene, which shows the promise of extending the use of PVDF membranes to nanofiltration processes, especially in harsh environments.

Authorship contributions

‡These authors contributed equally. The manuscript was written through contributions of all authors.

Acknowledgement

This work is supported by the Engineering and Physical Sciences Research Council (EPSRC) UK (grant EP/M01486X/1). The XRD data was analyzed using CrystalMaker®, CrystalMaker Software Ltd, http://www.crystalmaker.com. XPS data collection was performed at the EPSRC National Facility for XPS ("HarwellXPS"), operated by Cardiff University and UCL, under contract No. PR16195.

References

[1] A. Schaefer, A.G. Fane, T.D. Waite, Nanofiltration: Principles and Applications, Elsevier Science, 2005.
[2] L.W. Jye, A.F. Ismail, Nanofiltration membranes: Synthesis, characterization, and applications, Crc Press, 2016.
[3] A. Asatekin, A. Menniti, S.T. Kang, M. Elimelech, E. Morgenroth, A.M. Mayes, Antifouling nanofiltration membranes for membrane bioreactors from self-assembling graft copolymers, J Membr Sci, 285 (2006) 81-89.
[4] J. Wang, S. Zhang, P. Wu, W. Shi, Z. Wang, Y. Hu, In situ surface modification of thin-film composite polyamide membrane with zwitterions for the enhanced chlorine-resistance and transport properties, Acs Appl Mater Interf, (2019).
[5] Runlin, Han, Formation and characterization of (melamine–TMC) based thin film composite NF membranes for improved thermal and chlorine resistance, J Membr Sci, (2013).
[6] W.J. Lau, A.F. Ismail, N. Misdan, M.A. Kassim, A recent progress in thin film composite membrane: A review, Desal, 287 (2012) 190-199.
[7] S. Bing, J. Wang, H. Xu, Y. Zhao, Y. Zhou, L. Zhang, C. Gao, L.A. Hou, Polyamide thin-film composite membrane modified with persulfate for improvement of perm-selectivity and chlorine-resistance, J Membr Sci, 555 (2018) 318-326.
[8] F. Liu, N.A. Hashim, Y.T. Liu, M.R.M. Abed, K. Li, Progress in the production and modification of PVDF membranes, J Membr Sci, 375 (2011) 1-27.
[9] G.D. Kang, Y.M. Cao, Application and modification of poly(vinylidene fluoride) (PVDF) membranes - A review, J Membr Sci, 463 (2014) 145-165.

[10] J. Ji, F. Liu, N.A. Hashim, M.R.M. Abed, K. Li, Poly(vinylidene fluoride) (PVDF) membranes for fluid separation, React Funct Polym, 86 (2015) 134-153.
[11] L.R. Firman, N.A. Ochoa, J. Marchese, C.L. Pagliero, Deacidification and solvent recovery of soybean oil by nanofiltration membranes, J Membr Sci, 431 (2013) 187-196.
[12] F. Yuan, Y. Yang, R. Wang, D.J. Chen, Poly(vinylidene fluoride) grafted polystyrene (PVDF-g-PS) membrane based on in situ polymerization for solvent resistant nanofiltration, Rsc Adv, 7 (2017) 33201-33207.
[13] S.J. Park, R.K. Cheedrala, M.S. Diallo, C. Kim, I.S. Kim, W.A. Goddard, Nanofiltration membranes based on polyvinylidene fluoride nanofibrous scaffolds and crosslinked polyethyleneimine networks, J Nanopart Res, 14 (2012).
[14] J.Q. Liu, Z.L. Xu, X.H. Li, Y. Zhang, Y. Zhou, Z.X. Wang, X.J. Wang, An improved process to prepare high separation performance PA/PVDF hollow fiber composite nanofiltration membranes, Sep Purif Technol, 58 (2007) 53-60.
[15] M. Mertens, C. Van Goethem, M. Thijs, G. Koeckelberghs, I.F.J. Vankelecom, Crosslinked PVDF-membranes for solvent resistant nanofiltration, J Membr Sci, 566 (2018) 223-230.
[16] M.G. Buonomenna, L.C. Lopez, P. Favia, R. d'Agostino, A. Gordano, E. Drioli, New PVDF membranes: The effect of plasma surface modification on retention in nanofiltration of aqueous solution containing organic compounds, Water Res, 41 (2007) 4309-4316.
[17] C.S. Guo, H.T. Shi, W. Wang, X.Y. Pei, K.Y. Teng, Y.L. Hu, Z.W. Xu, H. Deng, X.M. Qian, Improvement of PVDF nanofiltration membrane potential, separation and anti -fouling performance by electret treatment, Sci Total Environ, 722 (2020).
[18] G.Y. Zeng, Y. He, Y.Q. Zhan, L. Zhang, Y. Pan, C.L. Zhang, Z.X. Yu, Novel polyvinylidene fluoride nanofiltration membrane blended with functionalized halloysite nanotubes for dye and heavy metal ions removal, J Hazard Mater, 317 (2016) 60-72.
[19] K. Ekambaram, M. Doraisamy, Surface modification of PVDF nanofiltration membrane using Carboxymethylchitosan-Zinc oxide bionanocomposite for the removal of inorganic salts and humic acid, Colloid Surf A, 525 (2017) 49-63.
[20] N. Nikooe, E. Saljoughi, Preparation and characterization of novel PVDF nanofiltration membranes with hydrophilic property for filtration of dye aqueous solution, Appl Surf Sci, 413 (2017) 41-49.
[21] S. Li, H. Wang, D.D. Li, X.D. Zhang, Y.F. Wang, J.F. Xie, J.Y. Wang, Y.P. Tian, W.X. Ni, Y. Xie, Siloxene nanosheets: a metal-free semiconductor for water splitting, J Mater Chem A, 4 (2016) 15841-15844.
[22] K. Krishnamoorthy, P. Pazhamalai, S.J. Kim, Two-dimensional siloxene nanosheets: novel high-performance supercapacitor electrode materials, Energ Environ Sci, 11 (2018) 1595-1602.
[23] N.F. Rosli, N. Rohaizad, J. Sturala, A.C. Fisher, R.D. Webster, M. Pumera, Siloxene, germanane, and methylgermanane: Functionalized 2D materials of group 14 for electrochemical applications, Adv Funct Mater, 30 (2020).
[24] R.S. Fu, K.L. Zhang, R.P. Zaccaria, H.R. Huang, Y.G. Xia, Z.P. Liu, Two-dimensional silicon suboxides nanostructures with Si nanodomains confined in amorphous SiO2 derived from siloxene as high performance anode for Li-ion batteries, Nano Energy, 39 (2017) 546-553.
[25] Z.X. Low, J. Ji, D. Blumenstock, Y.M. Chew, D. Wolverson, D. Mattia, Fouling resistant 2D boron nitride nanosheet - PES nanofiltration membranes, J Membr Sci, 563 (2018) 949-956.

[26] E. Nightingale Jr, Phenomenological theory of ion solvation. Effective radii of hydrated ions, J Phys Chem, 63 (1959) 1381-1387.
[27] G.M. Geise, D.R. Paul, B.D. Freeman, Fundamental water and salt transport properties of polymeric materials, Progress Polym Sci, 39 (2014) 1-42.
[28] J.C. Meyer, A. Chuvilin, G. Algara-Siller, J. Biskupek, U.J.N.L. Kaiser, Selective sputtering and atomic resolution imaging of atomically thin boron nitride membranes, Nano Lett., 9 (2009) 2683-2689.
[29] S. Bonnamy, A. Oberlin, Chapter 4 - Transmission Electron Microscopy, in: M. Inagaki, F. Kang (Eds.) Materials Science and Engineering of Carbon, Butterworth-Heinemann, 2016, pp. 45-70.
[30] H. Nakano, M. Ishii, H. Nakamura, Preparation and structure of novel siloxene nanosheets, Chem Comm, (2005) 2945-2947.
[31] S. Yamanaka, H. Matsu, M. Ishikawa, New deintercalation reaction of calcium from calcium disilicide. Synthesis of layered polysilane, Mater Res Bull, 31 (1996) 307-316.
[32] H. Imagawa, N. Takahashi, T. Nonaka, Y. Kato, K. Nishikawa, H. Itahara, Synthesis of a calcium-bridged siloxene by a solid state reaction for optical and electrochemical properties, J Mater Chem A, 3 (2015) 9411-9414.
[33] H.D. Fuchs, M. Stutzmann, M.S. Brandt, M. Rosenbauer, J. Weber, A. Breitschwerdt, P. Deak, M. Cardona, Porous Silicon and Siloxene - Vibrational and structural-properties, Phys Rev B, 48 (1993) 8172-8183.
[34] J.R. Dahn, B.M. Way, E. Fuller, J.S. Tse, Structure of siloxene and layered polysilane (Si6h6), Phys Rev B, 48 (1993) 17872-17877.
[35] B.J. Ryan, M.P. Hanrahan, Y.J. Wang, U. Ramesh, C.K.A. Nyamekye, R.D. Nelson, Z.Z. Liu, C.K. Huang, B. Whitehead, J.G. Wang, L.T. Roling, E.A. Smith, A.J. Rossini, M.G. Panthani, Silicene, siloxene, or silicane? Revealing the structure and optical properties of silicon nanosheets derived from calcium disilicide, Chem Mater, 32 (2020) 795-804.
[36] C. Smolders, A. Reuvers, R. Boom, I. Wienk, Microstructures in phase-inversion membranes. Part 1. Formation of macrovoids, J Membr Sci, 73 (1992) 259-275.
[37] S. Mazinani, S. Darvishmanesh, A. Ehsanzadeh, B. Van der Bruggen, Phase separation analysis of Extem/solvent/non-solvent systems and relation with membrane morphology, J Membr Sci, 526 (2017) 301-314.
[38] Z. Yang, Y. Wu, H. Guo, X.-H. Ma, C.-E. Lin, Y. Zhou, B. Cao, B.-K. Zhu, K. Shih, C.Y. Tang, A novel thin-film nano-templated composite membrane with in situ silver nanoparticles loading: Separation performance enhancement and implications, J Membr Sci, 544 (2017) 351-358.
[39] H. Luo, X. Zhou, C. Ellingford, Y. Zhang, S. Chen, K. Zhou, D. Zhang, C.R. Bowen, C. Wan, Interface design for high energy density polymer nanocomposites, Chem Soc Rev, 48 (2019) 4424-4465.
[40] Y. Shen, A.C. Lua, Preparation and characterization of mixed matrix membranes based on poly(vinylidene fluoride) and zeolite 4A for gas separation, Polym Eng Sci, 52 (2012) 2106-2113.
[41] J. Ji, S.Y. Zhou, C.Y. Lai, B. Wang, K. Li, PVDF/palygorskite composite ultrafiltration membranes with enhanced abrasion resistance and flux, J Membr Sci, 495 (2015) 91-100.
[42] F. Liu, M.R.M. Abed, K. Li, Preparation and characterization of poly(vinylidene fluoride) (PVDF) based ultrafiltration membranes using nano gamma-Al2O3, J Membr Sci, 366 (2011) 97-103.

[43] X.M. Cai, T.P. Lei, D.H. Sun, L.W. Lin, A critical analysis of the alpha, beta and gamma phases in poly(vinylidene fluoride) using FTIR, Rsc Adv, 7 (2017) 15382-15389.
[44] S.H. Huang, C.C. Hu, K.R. Lee, D.J. Liaw, J.Y. Lai, Gas separation properties of aromatic poly(amide-imide) membranes, Eur Polym J, 42 (2006) 140-148.
[45] W.S. Hung, T.J. Lin, Y.H. Chiao, A. Sengupta, Y.C. Hsiao, S.R. Wickramasinghe, C.C. Hu, K.R. Lee, J.Y. Lai, Graphene-induced tuning of the d-spacing of graphene oxide composite nanofiltration membranes for frictionless capillary action-induced enhancement of water permeability, J Mater Chem A, 6 (2018) 19445-19454.
[46] L.F. Warren, J.A. Walker, D.P. Anderson, C.G. Rhodes, L.J. Buckley, A Study of Conducting Polymer Morphology - the Effect of Dopant Anions Upon Order, J Electrochem Soc, 136 (1989) 2286-2295.
[47] X. Zhang, B.-W. Li, L. Dong, H. Liu, W. Chen, Y. Shen, C.-W. Nan, Superior Energy Storage Performances of Polymer Nanocomposites via Modification of Filler/Polymer Interfaces, Adv Mater Interf, 5 (2018) 1800096.
[48] R. Atif, J. Khaliq, M. Combrinck, A.H. Hassanin, I. Shyha, Solution blow spinning of polyvinylidene fluoride based fibers for energy harvesting applications: A review, Polymers, 12 (2020) 1304.
[49] E. Nagy, Basic equations of the mass transport through a membrane layer, Elsev Insight, (2012) 1-329.
[50] I. Koyuncu, D. Topacik, Effect of organic ion on the separation of salts by nanofiltration membranes, J Membr Sci, 195 (2002) 247-263.
[51] P. Liu, C. Milletto, S. Monti, C.T. Zhu, A.P. Mathew, Design of ultrathin hybrid membranes with improved retention efficiency of molecular dyes, Rsc Adv, 9 (2019) 28657-28669.
[52] R. Joshi, P. Carbone, F.-C. Wang, V.G. Kravets, Y. Su, I.V. Grigorieva, H. Wu, A.K. Geim, R.R. Nair, Precise and ultrafast molecular sieving through graphene oxide membranes, Science, 343 (2014) 752-754.
[53] T. Kurucsev, A. Sargeson, B. West, Size and hydration of inorganic macroions from viscosity and density measurements, J Phys Chem, 61 (1957) 1567-1569.
[54] S.G. Schultz, A. Solomon, Determination of the effective hydrodynamic radii of small molecules by viscometry, J Gener Physiol, 44 (1961) 1189-1199.
[55] L.A. Richards, A.I. Schäfer, B.S. Richards, B. Corry, The importance of dehydration in determining ion transport in narrow pores, Small, 8 (2012) 1701-1709.
[56] M.L. Connolly, Solvent-accessible surfaces of proteins and nucleic acids, Science, 221 (1983) 709-713.
[57] M.L. Connolly, The molecular surface package, J Molecul Graphics, 11 (1993) 139-141.
[58] A. Akbari, P. Sheath, S.T. Martin, D.B. Shinde, M. Shaibani, P.C. Banerjee, R. Tkacz, D. Bhattacharyya, M. Majumder, Large-area graphene-based nanofiltration membranes by shear alignment of discotic nematic liquid crystals of graphene oxide, Nat Commun, 7 (2016).
[59] N. Stafie, D.F. Stamatialis, A. Wessling, Insight into the transport of hexane-solute systems through tailor-made composite membranes, J Membr Sci, 228 (2004) 103-116.
[60] D. Bhanushali, S. Kloos, C. Kurth, D. Bhattacharyya, Performance of solvent-resistant membranes for non-aqueous systems: solvent permeation results and modeling, J Membr Sci, 189 (2001) 1-21.

[61] X. Li, B.L. Chen, W.B. Cai, T. Wang, Z. Wu, J.D. Li, Highly stable PDMS-PTFPMS/PVDF OSN membranes for hexane recovery during vegetable oil production, Rsc Adv, 7 (2017) 11381-11388.
[62] H.M. Krieg, S.J. Modise, K. Keizei, H.W.J.P. Neomagus, Salt rejection in nanofiltration for single and binary salt mixtures in view of sulphate removal, Desal, 171 (2005) 205-215.
[63] L. Wang, X.J. Song, T. Wang, S.Z. Wang, Z.N. Wang, C.J. Gao, Fabrication and characterization of polyethersulfone/carbon nanotubes (PES/CNTs) based mixed matrix membranes (MMMs) for nanofiltration application, Appl Surf Sci, 330 (2015) 118-125.
[64] V. Vatanpour, S.S. Madaeni, R. Moradian, S. Zinadini, B. Astinchap, Fabrication and characterization of novel antifouling nanofiltration membrane prepared from oxidized multiwalled carbon nanotube/polyethersulfone nanocomposite, J Membr Sci, 375 (2011) 284-294.
[65] J. Li, S.S. Yuan, J.Y. Zhu, B. Van der Bruggen, High-flux, antibacterial composite membranes via polydopamine-assisted PEI-TiO2/Ag modification for dye removal, Chem Eng J, 373 (2019) 275-284.
[66] Z. Yang, Z.-w. Zhou, H. Guo, Z. Yao, X.-h. Ma, X. Song, S.-P. Feng, C.Y. Tang, Tannic acid/Fe3+ nanoscaffold for interfacial polymerization: toward enhanced nanofiltration performance, Enviro Sci Tech, 52 (2018) 9341-9349.